Determination of Collar's Triangle of Forces on a Flexible Wing based on Particle Tracking Velocimetry Measurements

Mertens, C.; de Rojas Cordero, T.; Sodja, J.; Sciacchitano, A.; van Oudheusden, B.W.

DOI
10.2514/6.2021-0221

Publication date
2021

Document Version
Final published version

Published in
AIAA Scitech 2021 Forum

AIAA SciTech Forum
11–15 & 19–21 January 2021, VIRTUAL EVENT
AIAA Scitech 2021 Forum

10.2514/6.2021-0221

Determination of Collar's Triangle of Forces on a Flexible Wing based on Particle Tracking Velocimetry Measurements

Christoph Mertens*, Tomás de Rojas Cordero†, Jurij Sodja‡, Andrea Sciacchitano§ and Bas W. van Oudheusden¶
Faculty of Aerospace Engineering, Delft University of Technology, 2629 HS Delft, The Netherlands

The three components in Collar's triangle of forces (aerodynamic, elastic and inertial) acting on a flexible wing are determined, based on integrated optical measurements of the structural and the aerodynamic response to steady and unsteady periodic inflow conditions. The measurement device is a coaxial volumetric velocimeter mounted on a robotic arm, which is used to perform optical measurements of fiducial markers on the wing surface and simultaneously of helium-filled soap bubbles that are used as flow tracers. The optical measurements of the structural markers and the flow tracers are both processed with the Lagrangian particle tracking algorithm Shake-The-Box. Subsequently, physical models are used to determine the inertial and the elastic force of the aeroelastic interaction from the marker tracking results, and to determine the unsteady aerodynamic lift force from the flow velocity fields. The results of this integrated aeroelastic characterization approach are in physical agreement with each other according to the equilibrium of forces in Collar's triangle and good agreement with external reference measurements.

I. Nomenclature

c	=	Chord length
f	=	Frequency
i	=	imaginary unit
k	=	Reduced frequency
q	=	External load on the beam
s	=	Span width
w	=	Beam deflection
x	=	Streamwise coordinate
y	=	Crossflow coordinate
z	=	Spanwise coordinate
A	=	Aerodynamic force
E	=	Elastic force
EI	=	Flexural rigidity
I	=	Inertial force
L	=	Lift force
M	=	Bending moment in the beam
Q	=	Shear force in the beam
U_∞	=	Freestream velocity
$\mathbf{K}$	=	Stiffness matrix
$\mathbf{M}$	=	Mass matrix
$\mathbf{f}$	=	Finite element external force vector
$\boldsymbol{\xi}$	=	Finite element model degrees of freedom of the beam
α	=	Geometric angle of incidence of the wing
β	=	Angle of the gust vanes

*PhD student, Aerodynamics Department, C.Mertens@tudelft.nl
†Former MSc student, Aerodynamics Department
‡Senior researcher, Aerospace Structures and Materials Department
§Assistant professor, Aerodynamics Department
¶Associate professor, Aerodynamics Department

γ = Vortex sheet strength
Γ = Circulation
μ = Mass per unit span
ρ = Fluid density
σ = Standard deviation
φ = Phase lag
ω = Angular frequency
CVV = Coaxial volumetric velocimetry probe
HFSB = Helium-filled soap bubbles
OJF = Open jet facility wind tunnel
PTV = Particle tracking velocimetry
RMS = Root mean square value

II. Introduction

Aeroelasticity is a highly relevant field in aeronautics research, which has to be considered to ensure the desired operation and performance characteristics, as well as the safety of an aircraft design. There are several aeroelastic phenomena, such as flutter, divergence and control reversal, which can cause catastrophic failures on aircraft and consequently have been studied for around one century now [1]. A popular concept to depict the field of aeroelasticity and categorize the problems that occur within it is Collar's triangle of forces (see Fig. 1), introduced by A. R. Collar [2].

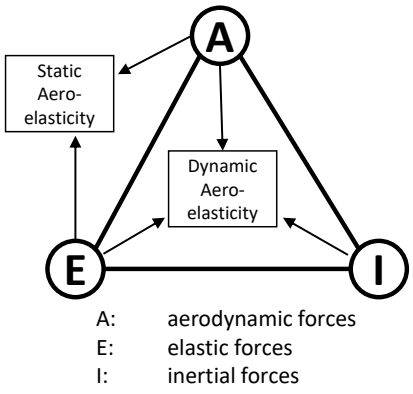

Fig. 1 Collar's triangle of forces, reproduced from [2]

The schematic represents graphically the interaction of the three forces involved in aeroelasticity, which are the aerodynamic, elastic and inertial forces. The different nature of these forces makes it difficult to analyze the dynamic aeroelastic response of aircraft structures; analytical models exist to predict the occurrence of certain aeroelastic phenomena like flutter [3], but the multidisciplinary nature makes wind tunnel experiments for investigating aeroelastic phenomena and validating the model predictions challenging to perform. A variety of measurement instruments for the determination of the individual forces is available (e.g. pressure transducers, accelerometers, load cells), but their coordinated use results in complex and expensive experimental setups. Additionally, installed sensors are invasive to the experimental model, locally changing its shape and/or mass, while providing only discrete information, typically with a relatively low spatial resolution. As a result, experimental reference data from wind tunnel measurements that can be used for the comparison with theoretical results and for calibrating computational models are typically limited to only a few quantities that are relatively easy to obtain, such as the wingtip deflection or the frequency of the dynamic motion [4].

Modern optical measurement techniques, such as particle image or tracking velocimetry (PIV/PTV, [5]) for aerodynamics and digital image correlation (DIC, [6]) for structural dynamics, provide non-invasive field measurements and hence overcome many of the particular limitations associated with the use of installed sensors. The potential of the combined use of these techniques in aeroelasticity experiments is demonstrated in [7], where PIV and DIC were used to simultaneously determine the deformation of a flexible wing and the resulting unsteady position of the wingtip vortex. Similarly, the deformation and aerodynamic loads on a flexible plate were investigated in [8] using DIC and PIV,

respectively. These existing studies indicate the capabilities of optical measurement techniques for the non-intrusive characterization of aeroelastic phenomena, but they do not overcome the complication of the coordinated use of several measurement and data processing systems, which would be a requirement for simple and fast production of aeroelastic reference data. This problem was approached for example in [9], where the aerodynamic force in terms of the surface pressure and the deformation of a flexible wing in transonic flow were determined in an integrated approach from pressure-sensitive paint images by using fiducial markers placed on the wing in a photogrammetric approach. However, while this approach facilitates the combined measurement of the aerodynamic and structural behavior with only one optical data acquisition system, it requires two separate system calibrations and data processing methods to obtain these measurements.

The current study proposes the use of PTV to determine all three forces in Collar's triangle with a non-intrusive, integrated measurement approach, using only one measurement system that requires minimal instrumentation of the experimental model. The experimental model that is investigated in this study is a flexible wing, that is subjected to steady and unsteady periodic inflow conditions. The unsteady periodic inflow is produced with a gust generator that performs a continuous sinusoidal motion upstream of the flexible wing. Optical measurements of the unsteady flow field and the structural motion are performed in an integrated manner, using the same PTV data acquisition and processing system. Particle tracking velocimetry via the Lagrangian particle tracking algorithm Shake-The-Box [10] using helium-filled soap bubbles as flow tracers [11] is a technique that is suitable for the measurement of large-scale unsteady flow fields [12–14] and can also be used to perform photogrammetric tracking of fiducial markers on moving objects in the flow [15]. After the PTV measurements of the flow and the structural motion are obtained, physical models need to be applied to determine the unsteady interaction of the forces of different nature on the wing. The identification of suitable procedures to determine the loads based on experimental measurements of the flow velocity and the structural deformation by using physical models is the subject of ongoing research, see e.g. [16, 17] and [18], respectively. In this study, relatively simple physical models are used to demonstrate the experimental determination of Collar's triangle of forces for the investigated static and dynamic aeroelasticity test cases.

III. Physical models for the Determination of the Forces

A. Determination of the Aerodynamic Force

The component of the aerodynamic force that predominantly determines the aeroelastic response of a flexible wing is the normal force, which acts perpendicular to the airfoil chord. The geometric angle of attack $\alpha = 5°$ of the wing in this study can be considered sufficiently small, such that $\cos\alpha \approx 1$, while at the same time the drag force is considerably smaller than the lift. As a consequence, the lift force L, which acts perpendicular to the direction of the undisturbed inflow x, and the normal force are treated as equivalent in this study, while the drag force is not further taken into account. The lift per unit span L' of a thin airfoil in steady flow can be determined from the Kutta-Joukowsky theorem, based on the assumption of inviscid, incompressible and irrotational flow [19]:

$$L' = \rho U_\infty \Gamma. \tag{1}$$

The circulation Γ is be obtained from the measured flow velocity field $\vec{u}$ with a line integral over a closed path C around the airfoil:

$$\Gamma = -\oint_C \vec{u} \cdot d\vec{s}\,. \tag{2}$$

While the Kutta-Joukowsky theorem was originally derived for steady and irrotational flow, previous studies have observed that it is well-suited to determine the lift force from experimental measurements also in flow conditions where relatively small regions of the flow are not irrotational due to viscous boundary layer effects [20, 21]. As no large flow separation effects occur in the measured flow fields, it can be expected that the Kutta-Joukowsky theorem is a suitable approach to determine the lift force in the current study for the case of steady inflow.

In unsteady inflow conditions, the flow acceleration effects on the unsteady lift have to be considered in addition to the quasi-steady lift due to the circulation that is given by Eq. 1. Following the unsteady potential flow theory [22], the unsteady lift $L'(t)$ on a thin airfoil is given as

$$L'(t) = \rho U_\infty \Gamma(t) + \rho \int_0^c \left(\frac{\partial}{\partial t} \int_0^x \gamma(\tilde{x}, t) d\tilde{x} \right) dx\,. \tag{3}$$

The evaluation of the unsteady flow acceleration term, given as the second term in Eq. 3, requires knowledge of the temporal behavior of the distribution of the strength of the bound vortex sheet γ along the camber line, that represents the airfoil in the unsteady potential flow model. This expression can be simplified by using Stokes' theorem to replace the integral of the bound vortex sheet with the distribution of the circulation Γ along the chord:

$$L'(t) = \rho U_\infty \Gamma(t) + \rho \int_0^c \left(\frac{\partial}{\partial t} \Gamma(x,t) \right) dx \,. \tag{4}$$

The circulation distribution along the chord $\Gamma(x,t)$ is obtained similarly to the overall circulation around the wing $\Gamma(t)$, by line integrals of the measured flow velocity. The value of the circulation at a given chord position x_i is obtained by performing a line integral of the velocity along a contour that encloses the chord of the wing from the leading edge until x_i, at which point the line integration path begins and ends on the airfoil surface.

B. Determination of the Inertial Force

The dominant motion degree of freedom of the considered aeroelastic interaction is the deflection w, in the y-direction perpendicular to the chord line of the flexible wing. Therefore, a simplified model of the wing is considered, where the other motion degrees of freedom are not taken into account. It follows that the inertial force per unit span I' on the wing can be determined as the product of mass density and acceleration along the spanwise direction z:

$$I'(z,t) = -\mu(z)\ddot{w}(z,t) \,, \tag{5}$$

where $\mu(z)$ is the linear density, and $\ddot{w}$ is the second temporal derivative of the wing deflection. In the case of steady inflow, $\ddot{w} = 0$ and thus $I'(z) = 0$. For the case of unsteady inflow, the periodic inflow conditions in this study, produced by the sinusoidal operation of the gust generator at a frequency of ω_g as described in Sec. IV, justify the assumption that the resulting aerodynamic loading on the wing is sinusoidal. Assuming that the structural response of the wing is linear, it follows that the dynamic response of the wing is sinusoidal as well, with the same frequency as the excitation ω_g. This means that the stationary part of the dynamic response of the wing can be written as

$$w(z,t) = w_0(z) + w_a(z) e^{(i\omega_g t + \varphi)} \,, \tag{6}$$

where $w_0(z)$ is the mean deflection, which is identical to the wing deflection in response to the steady inflow, and $w_a(z)$ is the dynamic deflection amplitude. The second temporal derivative of Eq. 6 is

$$\ddot{w}(z,t) = -\omega_g^2 w_a(z) e^{(i\omega_g t + \varphi)} \,. \tag{7}$$

The inertial load $I'(z)$ as given in Eq. 5 is determined in this study by performing a sinusoidal curve-fitting to the PTV-based marker displacements from their respective mean values over the period, to determine $w_a(z)$ as well as the phase lag φ, and thus $\ddot{w}(z)$ according to Eq. 7.

C. Determination of the Elastic Force

For the determination of the elastic force in this study, the flexible wing is modeled as an Euler-Bernoulli beam along the wingspan, where the analysis is restricted to the bending deflection $w(z)$ across the span. The wing is clamped at the root so that $w(z=0) = 0$ and $w'(z=0) = 0$ are used as Dirichlet boundary conditions in the beam model. The Euler-Bernoulli equation that establishes a relation between the deflection and the external load on the wing $q(z)$ in the static case is

$$\frac{\mathrm{d}^2}{\mathrm{d}z^2} \left(EI(z) \frac{\mathrm{d}^2 w(z)}{\mathrm{d}z^2} \right) = q(z) \,, \tag{8}$$

while the shear force $Q(z)$ and the bending moment $M(z)$ in the beam are

$$Q(z) = -\frac{\mathrm{d}}{\mathrm{d}z} \left(EI(z) \frac{\mathrm{d}^2 w(z)}{\mathrm{d}z^2} \right) \tag{9}$$

$$M(z) = -EI(z) \frac{\mathrm{d}^2 w(z)}{\mathrm{d}z^2} \,. \tag{10}$$

The effective flexural rigidity $EI(z)$ is assumed to be known for this study, by using the values of the Timoshenko beam model for the same wing that is used in [23], where it was observed to yield results that are in good agreement with experimental data obtained from wind tunnels tests. The effective flexural rigidity varies along the span so that a finite element beam model is used to solve Eq. 8. In the static case, the governing equation of the finite element beam model is

$$\mathbf{K}\boldsymbol{\xi} = \mathbf{D}\mathbf{f}\,, \tag{11}$$

where $\mathbf{K}$ is the stiffness matrix, $\mathbf{D}$ is the loading matrix, $\mathbf{f}$ is the external force vector, and the vector $\boldsymbol{\xi}$ contains the values of the degrees of freedom per node of the beam, which are the deflection and the rotation at the nodes. The continuous beam deflection $w(z)$ is calculated from the discrete values of the degrees of freedom by using Hermite splines, and $\mathbf{f}$ is determined by sampling the distribution of the external load $q(z)$ at the nodes of the finite element model. More details on the finite element method that was used in this study can be found in Sec. 3.5.3 in [24].

In this study, it is not feasible to determine the elastic force directly with Eq. 11 by using the optical deformation measurements for determining $\boldsymbol{\xi}$, because the deformation measurements are not available along the entire span and they are affected by measurement noise. Instead, the elastic force is determined by performing an optimization, in which the beam deflection $w(z)$ is calculated from the result for $\boldsymbol{\xi} = \mathbf{K}^{-1}\mathbf{D}\mathbf{f}$ in response to a given external load on the beam $q(z)$. The difference of the beam deflection to the wing displacement measurements with PTV at the respective spanwise location is then minimized numerically, by performing an optimization of the load $q(z)$. Due to the relatively small spanwise region where measurements are available and the presence of the measurement noise in the PTV measurements, it is necessary to make an assumption of the behavior of the external load across the span to achieve sensible results with this approach. In this study, it is assumed that the external load on the beam is constant across the span with $q(z) = q_0$ so that q_0 is the only optimization variable. This assumption can be justified when considering that the wing is not tapered and that the external load is equivalent to the aerodynamic lift, while the lift reduction effects due to downwash near the wingtip are neglected based on the relatively large aspect ratio of the wing.

Following the optimization procedure for q_0 in the static case, the shear force and the bending moment in the beam are determined with Eq. 9 and 10, which can be solved analytically in the case of a given constant external load in the static case, when considering the Neumann boundary conditions $Q(z = s) = 0$ and $M(z = s) = 0$ at the free end:

$$Q(z) = -\int q_0\, dz = -q_0(z - s) \tag{12}$$

$$M(z) = \int Q(z)\, dz = -\frac{q_0}{2}(z^2 - 2zs + s^2)\,. \tag{13}$$

In the case that the wing is moving dynamically, the governing equation for the Euler-Bernoulli beam is

$$\frac{\partial^2}{\partial z^2}\left(EI(z)\frac{\partial^2 w(z,t)}{\partial z^2}\right) + \mu(z)\frac{\partial^2 w(z,t)}{\partial t^2} = q(z,t)\,, \tag{14}$$

and for the finite element model of the beam

$$\mathbf{K}\boldsymbol{\xi}(t) + \mathbf{M}\ddot{\boldsymbol{\xi}}(t) = \mathbf{D}\mathbf{f}(t)\,, \tag{15}$$

where $\mathbf{M}$ is the mass matrix, as determined from the mass distribution properties of the experimental model. In this case, the finite element equation can generally be solved for $\boldsymbol{\xi}(t)$ and hence $w(z,t)$ in response to a given, arbitrary loading $q(z,t)$ only numerically, under the condition that the initial conditions for $\boldsymbol{\xi}(t = 0)$ and $\dot{\boldsymbol{\xi}}(t = 0)$ are known.

In the assumed case of a loading given by $\mathbf{f}(t) = \mathbf{f}_0 + \mathbf{f}_a e^{i\omega_g t}$, the response is $\boldsymbol{\xi}(t) = \boldsymbol{\xi}_0 + \boldsymbol{\xi}_a e^{i\omega_g t}$, where the mean value of the dynamic response is equal to the static response to the mean forcing, $\mathbf{K}\boldsymbol{\xi}_0 = \mathbf{f}_0$, which can be assumed to be identical to the external load in the case of steady inflow, corresponding to q_0. It follows that Eq. 15 can be used to relate the external load amplitude $\mathbf{f}_a$ to the dynamic wing response amplitude $\boldsymbol{\xi}_a$ in a form that that does not depend on the time explicitly:

$$\left(\mathbf{K} - \omega_g^2\mathbf{M}\right)\boldsymbol{\xi}_a = \mathbf{D}\mathbf{f}_a\,. \tag{16}$$

Similar to the steady case, Eq. 16 is used in this study to optimize for the amplitude q_a of a sinusoidal, spanwise constant external load by fitting the finite element model beam deflection due to a given load to the wing deformation

amplitude, that is obtained from the experimental measurements. In this case, it is not trivial to derive analytical expressions for the shear force and the bending moment in the beam so that in the test case with unsteady inflow, these quantities are computed from second-order accurate finite differences, based on Eq. 9 and 10.

IV. Experimental Setup

A. Wind Tunnel Setup

The experiments were conducted in TU Delft's Open Jet Facility (OJF), which is a closed-loop, open test section wind tunnel with an octagonal exit of 2.85 m × 2.85 m. The wind tunnel is powered by a 500 kW electric motor which drives a fan that can provide freestream velocities of up to 35 m s^{-1} in the test section. In this study, the freestream velocity was set to $U_\infty = 14\,\mathrm{m\,s^{-1}}$, which corresponds to a Reynolds number of around 230 000 based on the chord of the flexible wing. The wind tunnel setup is shown in Fig. 2.

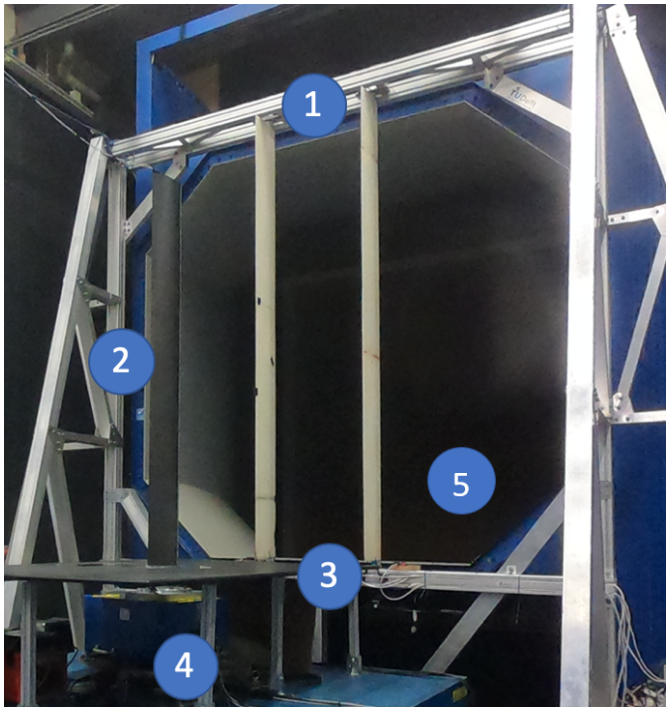

Fig. 2 Photo of the wind tunnel setup. 1: Gust generator mounted at the wind tunnel nozzle exit, 2: Flexible wing model, 3: Ground plate, 4: Six-component balance, 5: Helium-filled soap bubbles seeding generator (not visible in the photo, placed in the wind tunnel settling chamber)

For this study, a gust generator is mounted at the wind tunnel nozzle exit, which can generate various types of unsteady inflow to the model in the test section [25]. Two experimental test cases are considered in this study: one test case with steady inflow, where the gust generator is not operated, and a second test case with periodic unsteady inflow, where the gust generator is operated continuously with a sinusoidal variation of the gust vanes angle β according to $\beta(t) = 5° \times \sin(\omega_g t)$, where $\omega_g = 2\pi f_g$ is the angular frequency of the gust vane motion. The selected frequency of $f_g = 2\,\mathrm{Hz}$ corresponds to a reduced frequency of $k = (\pi \times c)/U_\infty = 0.11$ and is expected to cause considerable unsteady aerodynamic effects on the flexible wing model [26].

To perform the PTV measurements of the flow, the freestream is seeded with helium-filled soap bubble (HFSB) flow tracers with a diameter of about 0.5 mm. The HFSB are generated by a seeding generator, that consists of 200 bubble-producing nozzles over an area of 0.5 m × 1 m. The working principle of the bubble-producing nozzles is described in [27]. To improve the seeding concentration and to minimize the influence of the seeding generator on the turbulence intensity of the freestream, the seeding generator is placed in the settling chamber of the wind tunnel, upstream of the contraction of the wind tunnel nozzle.

B. Flexible Wing Model

The experimental model is a rectangular wing with a chord length of $c = 0.25$ m, a span width of $s = 1.75$ m and a NACA 0010 profile, that is oriented at a geometric angle of attack of $\alpha = 5°$ with respect to the freestream. The wing was made in-house out of carbon fiber reinforced epoxy unidirectional tailored laminates. Its inner structure is formed by two spars and thirteen ribs, and the outer skin is divided into three spanwise regions of equal length, where each has different laminate properties in terms of orientation and thickness. The properties of those laminates were determined through an optimization process, that was driven by an objective function to minimize the weight of the wing and to maximize the wing tip displacement under the flow conditions achievable in the OJF. The design and manufacturing procedure of the flexible wing model is described in detail in [23]. To enable the PTV measurements of the wing displacement, a rectangular grid of white circular markers is spray-painted on the surface of the wing model, using a laser-cut template. The markers have a diameter of 1.5 mm and the grid spacing is 30 mm. A sketch of the wing dimensions with the marker grid is shown in Fig. 3.

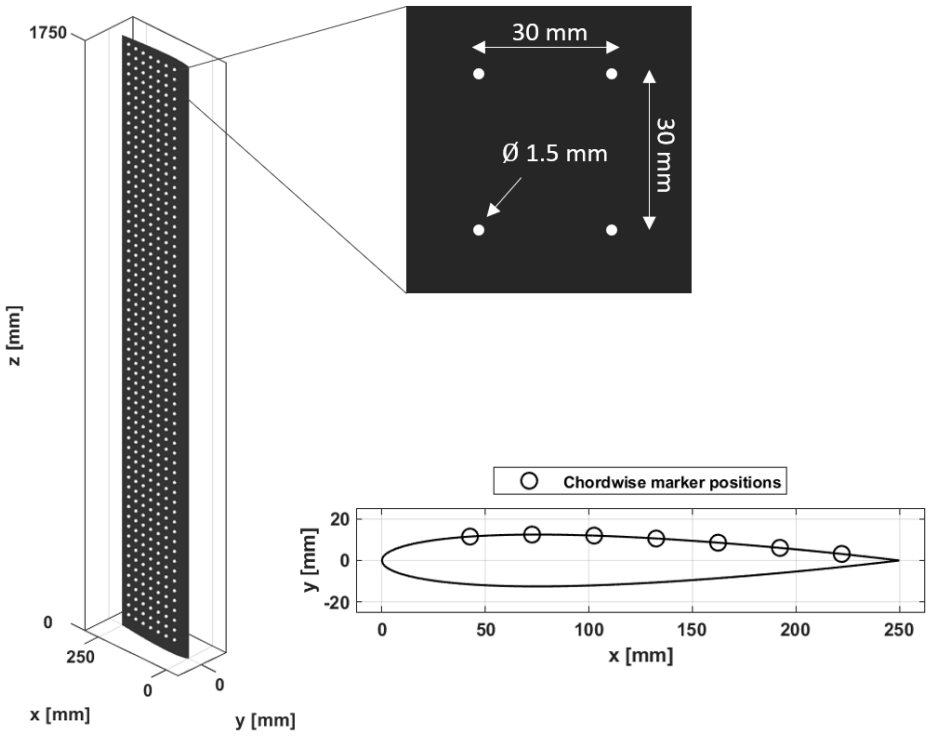

Fig. 3 a) Illustration of the wing model geometry with the fiducial marker grid, b) Chordwise positions of the fiducial markers on the wing surface

The flexible wing model is mounted on a six-component balance with a clamp arrangement that consists of an aluminum block that is glued to the bottom of the wing. The mass of the wing without the aluminum block is 1.44 kg. The dynamic motion amplitude of the flexible wing in response to the unsteady inflow generated by the gust vanes is increased by inserting a wingtip mass of 0.40 kg, which brings the natural frequencies of the wing closer to the excitation frequency achievable with the gust generator, thus generating larger dynamic wing deformations. With the experimental parameters employed in this study, the maximum wingtip deflection is around 40 mm, corresponding to around 2% of the span.

The measurements of the six-component balance on which the wing is mounted are used for validation purposes of the loads at the root of the wing, as determined with the beam model based on the PTV measurements. Additionally, the wing model is equipped with a LUNA HD6 fiber optic strain sensor, that is mounted at mid-chord on the inside of the pressure side of the wing, from the root until $z = 1.65$ m. The strain measurements from the optical fiber installed in the wing are obtained with a LUNA ODiSI data acquisition system and are used for validating the strains that are obtained from fitting the Euler-Bernoulli beam model to the PTV marker measurements.

C. Particle Tracking Velocimetry System

The primary measurement component that is used for the PTV measurements is a *LaVision MiniShaker Aero* coaxial volumetric velocimetry probe (CVV, [28]). The CVV features four CMOS cameras for image acquisition, that are mounted in a compact housing (dimensions 130 mm × 90 mm × 80 mm) together with the coaxial illumination component, which consists of an optical fiber with a diverging lens at the end to illuminate the particles in the field of view of the cameras. As illumination source, a Quantronix Darwin-Duo Nd:YLF laser (25 mJ pulse energy at 1 kHz, wavelength of 527 nm) is connected to the other end of the optical fiber. The compactness of the CVV probe allows it to be mounted on a Universal Robots UR5 robotic arm, which has six motion degrees of freedom and a maximum reach of 0.85 m. The controlled positioning in space of the CVV with the robotic arm enables the measurement of several adjacent volumes with the CVV without performing repeated calibrations and allows a simple combination of the measurement volumes in post-processing, which facilitates the measurement of flow fields around objects on a cubic meter scale [29]. The small tomographic aperture angle of the four CVV cameras causes relatively large random measurement errors along the viewing direction of the probe, which are around one order of magnitude larger than those in the vertical and horizontal directions in the image space, as described in [28].

V. Integrated Measurement Approach

A. PTV Data Acquisition

The setup for conducting the integrated aerodynamic and structural measurement is illustrated in Fig. 4. The stream of HSFB flow seeding, illuminated by the green laser light, is visible in between the CVV probe and the surface of the wing. The structural markers in the illuminated region are visible on the surface of the wing as well. The CVV is positioned in space with the robotic arm such that it is oriented at an angle of about 30% with respect to the cross-sectional x-y plane of the wing, so that direction of motion of neither the structural markers nor of the flow tracers is identical to the viewing axis of the CVV, where the random measurement error is the largest. For the chosen position and orientation of the CVV, that is shown in Fig. 4, measurements of the flow and the structure are obtained within the spanwise region of approximately $0.85 < z/s < 0.9$.

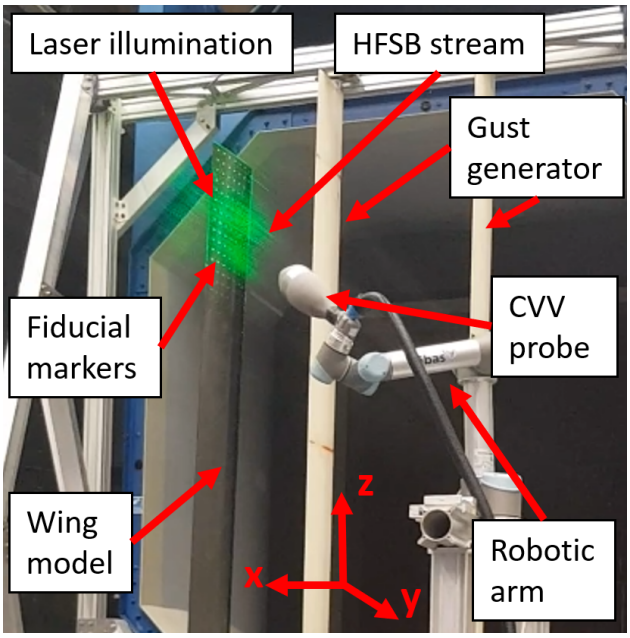

Fig. 4 Conducting of an integrated PTV measurement in the wind tunnel

The optical measurements of the flow and the structure are conducted with the maximum acquisition frequency of the CVV of $f_s = 821$ Hz and with the maximum camera sensor size for that acquisition frequency, which is 704 × 540 pixel. Six different positions of the CVV with respect to the wing are used to obtain measurements of the flow around the investigated wing section, see Fig. 5. To achieve this, the optical measurement setup is installed successively on both

sides of the wing, with three measurement volumes along the chord on the suction side (s) and three on the pressure side (p) of the wing. The combined size of the measurement volumes of this procedure is around 15 liters. For the case of steady inflow, 15,000 images are acquired per individual measurement volume. For the case of dynamic inflow, 98,520 images are acquired over 240 motion periods per measurement volume.

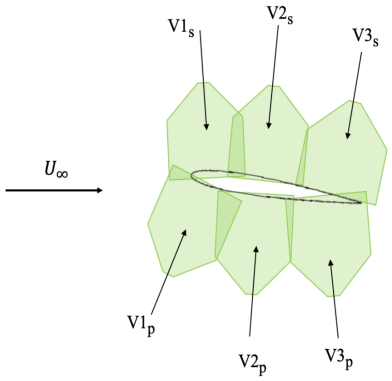

Fig. 5 Measurement volumes on the suction (s) and pressure (p) side of the wing

The processing procedure for the acquired data begins with the separation of the flow tracer information in the images from the structural marker information, as illustrated in Fig. 6. This step improves the performance of the PTV algorithm Shake-The-Box because the appearance of the structural markers and the flow tracers in the images is not identical (see Fig. 6); after the separation is performed, a non-uniform optical transfer function [30] can be generated for the structural markers and the flow tracers separately. The removal of the structural information from the integrated measurement images is achieved with a temporal high-pass filter [31], exploiting the different time scales of the structural motion and that of the flow. In principle, the reverse operation can be applied to obtain the image data of the structural markers without the flow tracer information using a temporal low-pass filter, as it was done in [15], however, in this study this step is not directly necessary, because the observed phenomena are either steady or periodic and thus repeatable over time. This means that the isolated structural marker information can be simply obtained by acquiring images without operating the HFSB seeding generator. This approach is advantageous because it allows the modification of the camera sensor size to the maximum of 704×636 pixel, which permits the simultaneous measurement of all markers along the chord with just one acquisition at a sampling frequency of $f_s = 500\,\text{Hz}$. These additional measurements of only the structural motion are conducted only on one side of the wing, using the position of the CVV that corresponds to V2p in Fig. 5. It is presumed that the measurements from the other side of the wing do not provide any additional information, given the relatively low density of the marker grid, the small deformation of the investigated spanwise region and the low fidelity of the physical model that is used to analyze these measurements, which does not consider shear deformations.

a) Raw image, structural markers and flow tracers

b) High pass filtered image, only flow tracers

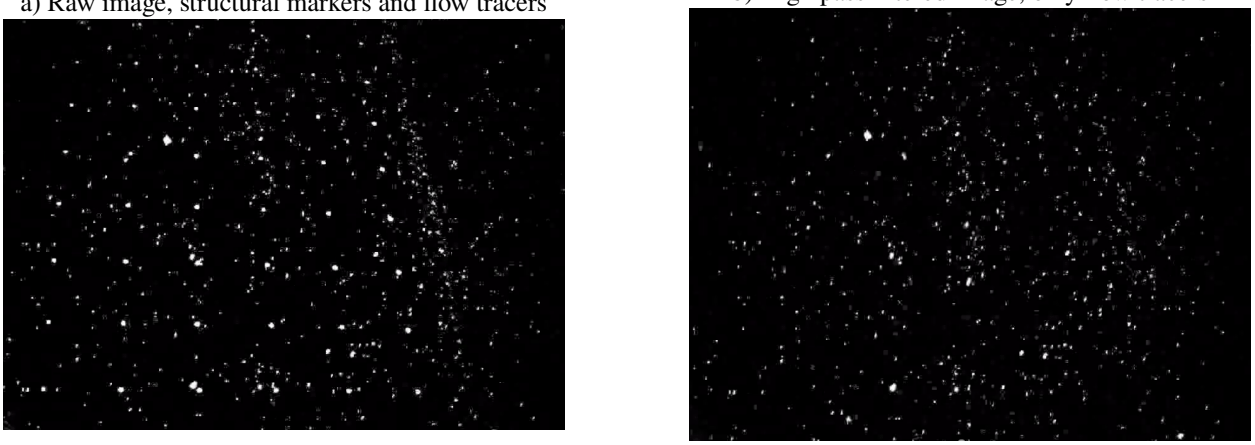

Fig. 6 Example for the image filtering procedure for separating flow tracer and structural marker information

B. PTV Data Processing

The complete data processing procedure that is followed in this study is illustrated in Fig. 7. After separating the flow and structural information, the next step is to apply the particle tracking algorithm. The used method for obtaining the PTV measurements consists of three steps, that are performed separately for the flow and the structure: first, a volume self-calibration [32] is performed, then an optical transfer function is generated, and afterwards the Shake-The-Box algorithm is applied. The results are obtained in terms of individual particle tracks, with position, velocity and acceleration of each particle over time, for both the structural markers and the flow tracers in separate files.

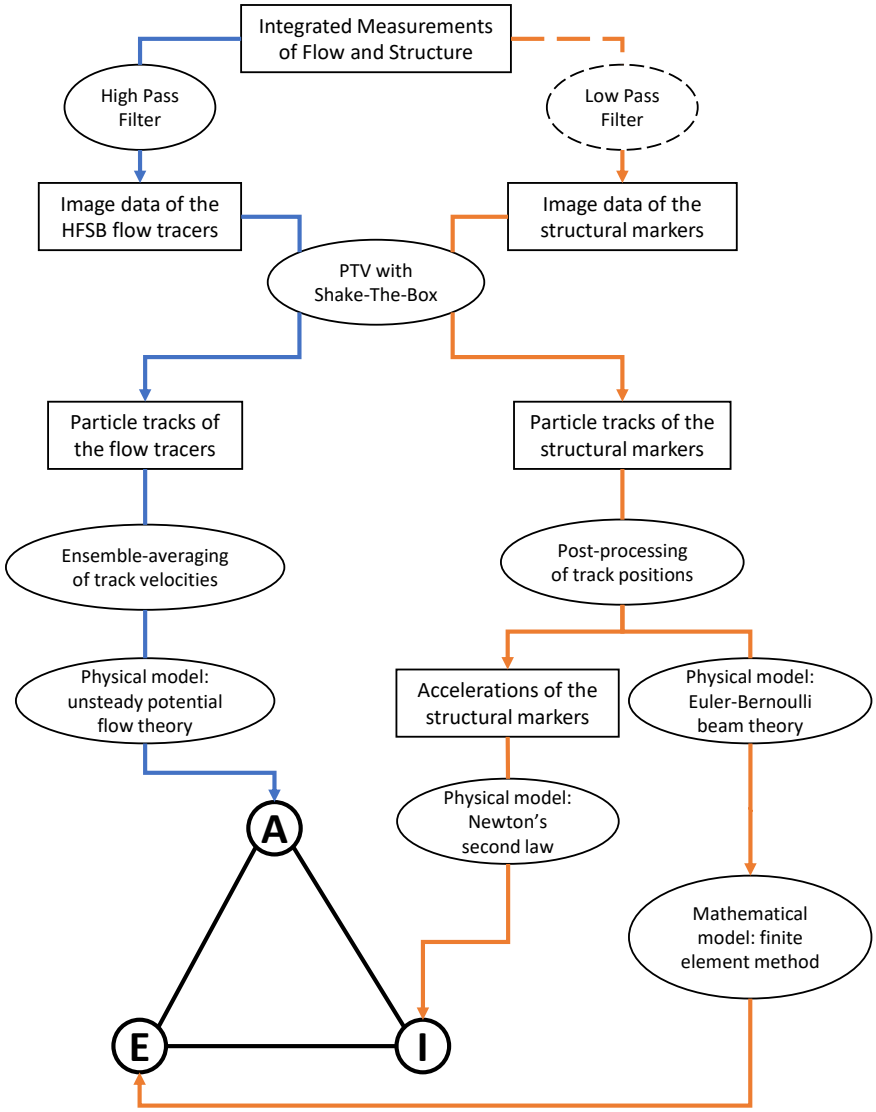

Fig. 7 Data processing procedure for the aerodynamic (blue) and structural measurements (orange)

After the track data of the flow tracers are obtained, the velocities of the flow tracer tracks are ensemble-averaged to a three-dimensional Cartesian grid with a spacing of 2.5 mm, using a top-hat filter approach with cubic bins of 10 mm × 10 mm × 10 mm, as described in [33]. For the measurements obtained in the case of steady inflow, the particle tracks obtained from all acquired images are combined in the ensemble-averaging procedure. For the measurements with dynamic periodic inflow, the particle tracks are ensemble-averaged in a phase-averaged sense based on the recorded signal of the gust generator motion, where the particle tracks are assembled in 100 temporal bins, each spanning 1% of the gust excitation period.

The particle tracks of the structural markers are processed in two different post-processing procedures for the cases of steady and unsteady inflow. In the case of steady inflow, the marker track positions within a radius of 10 mm are averaged to obtain the mean position of the observed grid of markers in space. The same procedure is then repeated for a reference measurement of the marker positions without wind tunnel operation. Subsequently, the difference between the two grids is calculated, to obtain the deflection of the wing. These results are then fitted to the physical model to determine the elastic forces as explained in Sec. III. For the analysis of the test case with unsteady inflow, only the amplitude of the deflection around the mean is required in the physical model for the determination of the inertial force and the elastic force, as the considered linear elastic theory suggests that the mean value of the deflection is given by the result for the case of steady inflow. The marker position measurements over time are phase-averaged in 100 temporal bins, which is identical to the processing parameters of the flow field so that the combination of the model position with the flow fields is coherent. The mean value of these position measurements per marker over the entire period is then subtracted from the phase-averaged positions to obtain the dynamic displacement of the respective marker over the cycle. In both test cases, no significant relation was observed between the chordwise position of the marker and the deflection, allowing the marker information to be averaged along the chord. This also supports the assumption that measuring on only one side of the wing is sufficient since the cross-section of the wing is not deforming. As shown in Fig. 7, the physical model for the determination of the elastic force requires the position measurements as input, while the determination of the inertial force requires measurements of the acceleration, which are computed from a sinusoidal fit to the phase-averaged position measurements.

C. Closure of Collar's Triangle

After the aerodynamic, the inertial and the elastic force are determined with the three described methods from the integrated measurements, the results can be combined in an internal validation procedure, where the physical agreement of the three different models with each other can be quantified. A free body diagram of a wing segment that is investigated between the spanwise stations z_1 and z_2 is shown in Fig. 8.

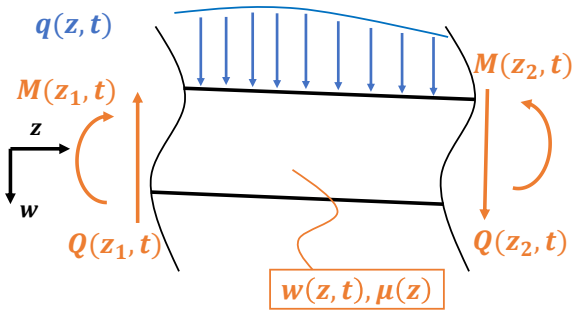

Fig. 8 Free body diagram of a wing section

The equilibrium of the forces in the direction of the deflection w in Fig. 8 is as follows:

$$\int_{z_1}^{z_2} \mu(z)\ddot{w}(z,t)dz = \int_{z_1}^{z_2} q(z,t)dz - Q(z_1,t) + Q(z_2,t)\,. \tag{17}$$

The three forces A, E, and I in Collar's triangle, that are involved in a dynamic aeroelastic interaction, can be recognized in Eq. 17:

$$A = \int_{z_1}^{z_2} L'(z,t)dz = \int_{z_1}^{z_2} q(z,t)dz \tag{18}$$

$$E = -Q(z_1,t) + Q(z_2,t) \tag{19}$$

$$I = \int_{z_1}^{z_2} I'(z,t)dz = -\int_{z_1}^{z_2} \mu(z)\ddot{w}(z,t)dz\,, \tag{20}$$

which means that the equilibrium of forces, that is given by Eq. 17, can be stated as $A + E + I = 0$ for the wing segment that is investigated in this study. This requirement is verified in this study by calculating a measurement residual, defined as $\delta = A + E + I$, which is then used to quantify the error of the considered approach.

VI. Results

A. Steady Inflow

For the test case with steady inflow, the aerodynamic force is determined from the measured flow velocity field and the elastic force is determined from the marker position measurements, while the inertial force is zero. The reaction force and moment at the root in the finite element model, which is used to determine the elastic force in the investigated wing section, can be validated against the balance measurements. The strain that results from the application of the determined external force to the beam model is compared with the optical strain fiber measurements. The elastic force on the segment is in equilibrium with the aerodynamic force in the absence of inertial forces so that a comparison of the two forces is performed and the residual of the considered approach is computed.

1. Elastic Force

The result for the deflection $w(z)$ of the finite element beam model as fitted to the PTV marker displacement measurements is shown in Fig. 9. The error bars on the measurements indicate the standard deviation σ in displacement for the seven chordwise markers that were used to produce one average displacement per spanwise position, which has values in the range of $0.28\,\text{mm} < \sigma < 0.61\,\text{mm}$. The agreement between the beam deflection and the chordwise-averaged marker displacement is very good, with a root mean square (RMS) value of the difference between measurement and model of 0.10 mm.

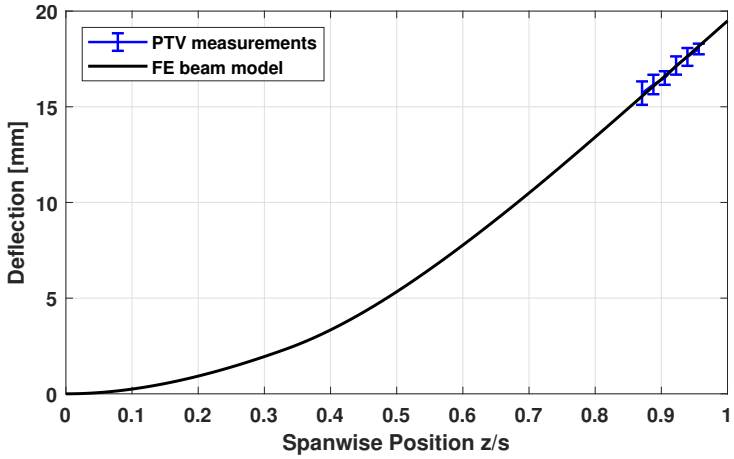

Fig. 9 Finite element beam model fitted to the static PTV measurements

The result for the deflected shape can be validated against the measurements from the optical strain fiber, that is installed inside the model surface on the pressure side of the wing. For this purpose, the strains according to the beam model are computed from the deflection line by using the equation for the strain of an Euler-Bernoulli beam:

$$\varepsilon = -\frac{d^2w}{dz^2}d\,, \tag{21}$$

where d is the distance of the optic fiber from the elastic axis of the beam, which is assumed to be on the chord line of the wing. The comparison between the strain measurement and the model strain is shown in Fig. 10. The cross-sectional stiffness properties of the wing change at $z/s = 1/3$ and $z/s = 2/3$, as described in [23], which results in a discontinuity of the strain in the beam model at these locations. In contrast, the strain fiber is installed on the inside of the pressure surface of the wing, where the stiffness properties only change at $z/s = 1/3$, and therefore the strain that is measured with the optical fiber is only discontinuous at that location and not at $z/s = 2/3$. Apart from this difference, the agreement between the model and the measurement is very good.

The influence of the finite element size on the optimization result q_0, the constant external load on the beam, is shown in Fig. 11. The model discretization of the considered finite element method is exact for a constant external load so that the sensitivity to the finite element size is very small. Differences are only caused by the interpolation with Hermite splines between the finite element nodes. This effect becomes negligible for more than six finite elements across the span (i.e. finite element size < 0.1 m), where the result for the external result is identical within 0.01%.

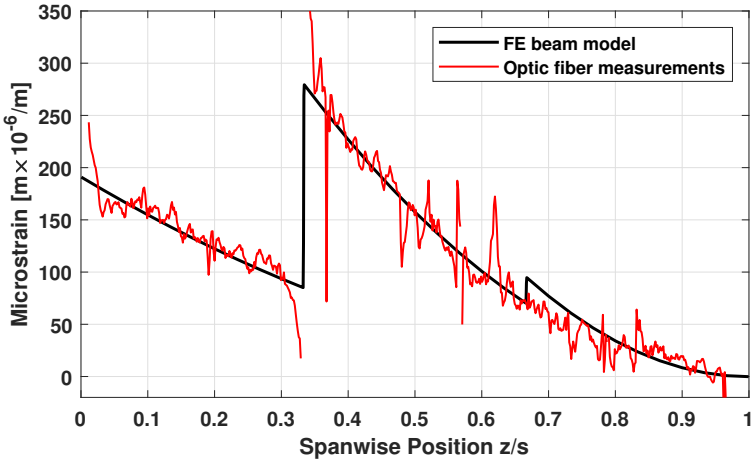

Fig. 10 Comparison of the strain from the finite element beam model with optic fiber measurements

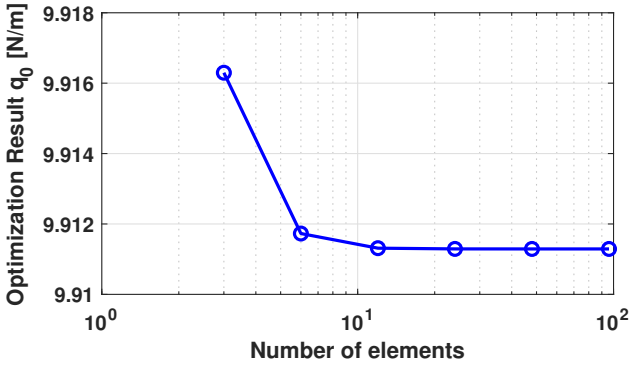

Fig. 11 Influence of the number of finite elements on the optimization result for q_0

After the external load q_0 is determined, the result can be used to calculate the shear force and the bending moment at the root of the flexible wing with Eq. 12 and 13. The value for the shear force can be directly compared to the force measurement of the balance, as shown in Tab. 1. For the comparison of the bending moment with the balance measurement, the height of the clamp arrangement h_{clamp} and the location of the balance center h_{balance} have to be considered as well. The root bending moment from the balance is determined from the balance measurements of the shear force and the moment under the assumption that no external bending moment is applied on the wing:

$$M(z=0)_{\text{balance}} = M_{\text{balance}} - Q_{\text{balance}} \times (h_{\text{clamp}} + h_{\text{balance}}) \tag{22}$$

Two different modeling assumptions are considered as the main sources for the observed differences in shear force and bending moment in Tab. 1. Firstly, to get reliable elastic forces, the stiffness model of the wing must be calibrated with measured data, that are obtained for example in a ground vibration test. This step has not been performed for this study. The second significant modeling assumption is that of a constant external load along the span. The validity of this assumption can be assessed by calculating the theoretical point of application R of a resultant force with the magnitude of the shear force at the wing root so that the bending moment at the root is identical:

$$R = \frac{M(z=0)}{Q(z=0)}. \tag{23}$$

The result for R is included in Tab. 1 as well. The balance measurements reveal that the resultant point of application is located slightly further inwards on the wingspan than in the assumed case of a spanwise-constant load, where R is located at mid-span, differing by about 5%. This indicates that the constant-load assumption is a reasonable approximation and not the dominant source of error in the considered approach.

Table 1 Comparison of model reaction forces at the root clamp with balance measurements

	Balance measurement	Finite element model	Relative error
Root shear force $Q(z = 0)$	-15.82 N	-17.34 N	9.64%
Root bending moment $M(z = 0)$	-13.20 N m	-15.18 N m	14.94%
Point of application R	$0.477 \times s$	$0.5 \times s$	4.84%

2. Aerodynamic Force

A section of the ensemble-averaged flow field, located at $z/s = 0.90$, is shown in Fig. 12, together with the position of the wing section that is determined from the marker position measurements. Furthermore, the black rectangle in the plot indicates an exemplary rectangular integration contour for the calculation of the circulation around the airfoil. The shown integration contour is positioned such that a minimum distance of 25 mm, which is equivalent to 0.1 chord lengths, to the surface of the wing is observed in all directions.

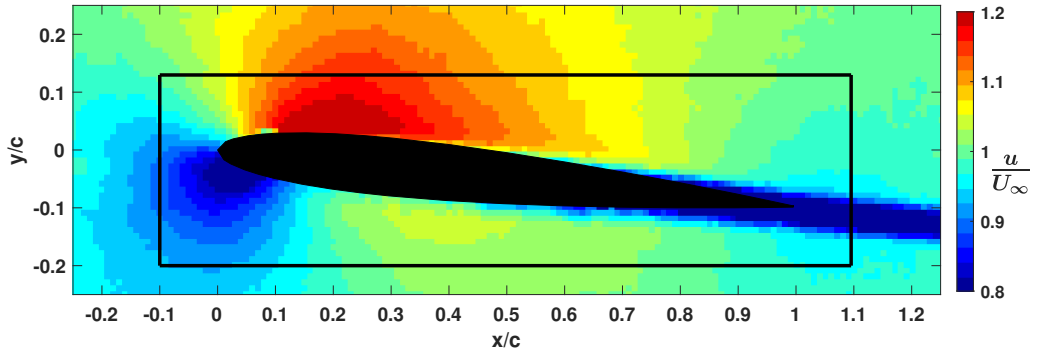

Fig. 12 Flow field, model position and circulation integration contour for steady inflow at z/s=0.90

The circulation measurement that is obtained from the flow field is used to calculate the section lift with the Kutta-Joukowsky theorem (Eq. 1), as shown for all spanwise sections where flow measurements were conducted in Fig. 13. In theory, the result for the lift is independent of the choice of the integration contour around the airfoil, which is used to determine the circulation. To reduce the sensitivity of the lift to the random error in the flow velocity measurements, the lift is therefore computed as the average of the lift values that are obtained when varying the distance of the rectangular integration contour to the wing surface from 0.05 to 0.2 chord lengths in $0.025c$ increments, for each spanwise position. No appreciable trend was observed with the variation of the position of the integration contour. The error bars in Fig. 13 indicate one standard deviation of these results for the lift.

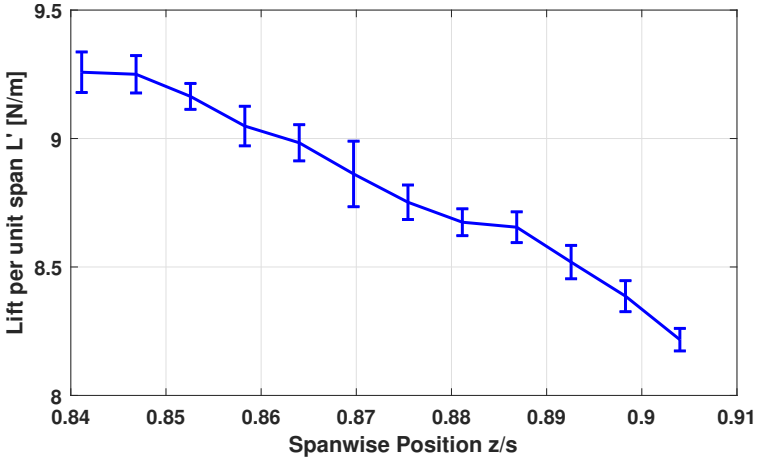

Fig. 13 Lift from the Kutta-Joukowsky theorem over the span

The aerodynamic force that is exerted on the investigated wing segment can be compared with the elastic force, that is determined from the marker measurements with the finite element model. When considering the wing segment between $z_1/s = 0.85$ and $z_2/s = 0.9$, the aerodynamic force on the segment can be calculated from the lift distribution shown in Fig. 13 with a trapezoidal integration:

$$A = \int_{z_1}^{z_2} L'(z)\, dz = 0.7691\,\mathrm{N}\,, \tag{24}$$

while the elastic force on the segment is:

$$E = -Q(z_1) + Q(z_2) = q_0(z_1 - z_2) = -0.8672\,\mathrm{N}\,. \tag{25}$$

According to the equilibrium of forces in Collar's triangle for the case of static aeroelasticity, the two forces A and E on the segment are equivalent in the absence of structural motion and hence inertial forces, which leads to the quantification of the observed measurement residual as $\delta = A + E = -0.0981$ N. The value for the measurement residual is used to calculate a relative error of the considered approach in the case of steady inflow. As a reference force, the balance measurement of the shear force at the root is scaled by the fraction of the investigated wing section, which is $(z_2 - z_1)/s = 0.05$. This yields a value for the relative error of $\epsilon = 12.41\%$ for the case of steady inflow, which is accredited to the difference between the elastic properties of the wing and the beam model and to the drop in lift towards the tip due to downwash effects, that is observed in Fig. 13, but not considered in the structural model.

B. Unsteady Periodic Inflow

For the dynamic aeroelastic test case with unsteady periodic inflow, all three forces in Collar's triangle have to be considered. The analysis of the dynamic structural motion is based on the assumption of a linear elastic response to a sinusoidal external forcing. The result of a sinusoidal fit to the marker position measurements can be used to validate this assumption and to determine the acceleration and hence the inertial force on the investigated wing segment. The amplitude of the marker displacement measurements is used to determine the amplitude of the dynamic elastic force with the finite element model. The unsteady aerodynamic force is determined from the measured flow fields and is subsequently compared to the inertial and elastic forces according to the equilibrium of forces in Collar's triangle.

1. Inertial Force

For the determination of the inertial force, the acceleration is determined from the phase- and chordwise averaged marker displacement measurements, by fitting a sinusoidal curve according to Eq. 6 through the measurements. The result is shown in Fig. 14, for two different marker positions along the span. The sinusoidal fit is a very good representation of the actual measurements, with an RMS of the difference between the fit and the measurements of around 0.2 mm, which is less than the typical standard deviation of the measurements during the phase- and chordwise averaging of the marker measurements, which is around 0.3 mm.

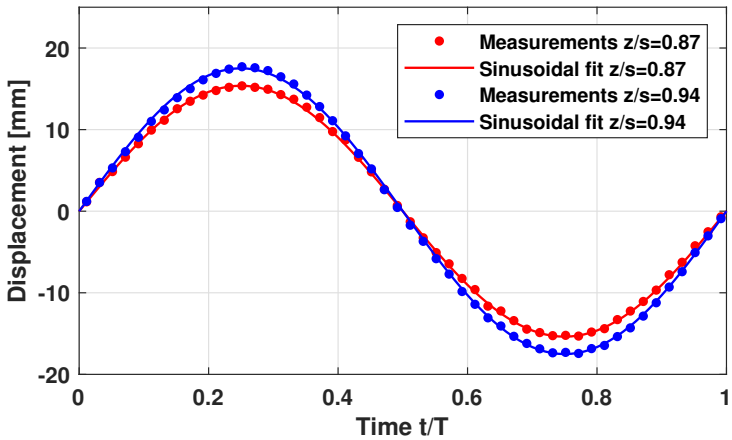

Fig. 14 Phase-averaged marker displacement from the mean for two spanwise locations

The spacing of the fiducial markers on the model of 30 mm, which corresponds to 1.7% of the span, is relatively coarse, and the bottom row of markers that are tracked during the entire motion cycle is at $z/s = 0.854$, which is within the region where the flow field is measured. Therefore, it is beneficial to use the discrete amplitude measurements, which are obtained at the spanwise positions of the fiducial markers as shown in Fig. 15, to estimate the continuous behavior of the wing motion in the investigated region. Because the measurements are performed near the tip, it can be assumed that the wing deformations are small and the measured amplitudes can be fitted with a linear curve, as shown in Fig. 15 as well.

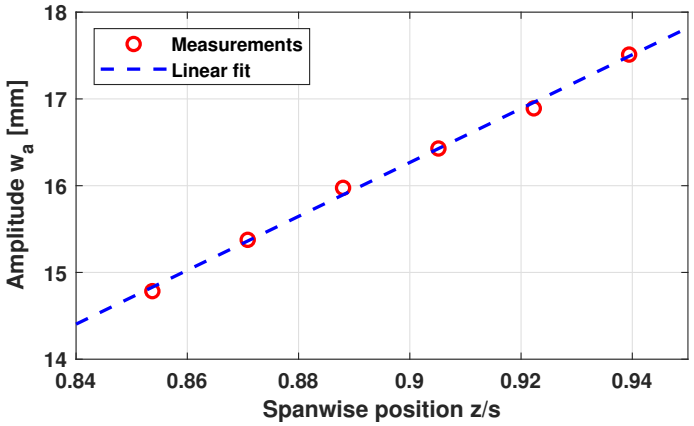

Fig. 15 Displacement amplitude over the span in the investigated region

With the obtained linear relation between the spanwise position on the investigated wing segment and the amplitudes of the sinusoidal fit according to Eq. 6, it is possible to determine the inertial forces on the segment between z_1 and z_2 with Eq. 7. Furthermore, the amplitude value of the linear fit at $z/s = 0.875$ is used for the determination of the elastic force in the following.

2. Elastic Force

For the determination of the elastic force in the dynamic case, the amplitude of the sinusoidal forcing q_a is determined from the observed wing motion amplitude w_a. For that, the finite element formulation of the dynamic beam bending motion in Eq. 16 is solved in an optimization procedure for q_a that minimizes the difference between model and measurement. The influence of the finite element size on the optimization result is shown in Fig. 16. Similar to the static case, the effect of the number of finite elements on the result for q_a diminishes already for a small number of elements and remains constant at 6.544 N m^{-1}.

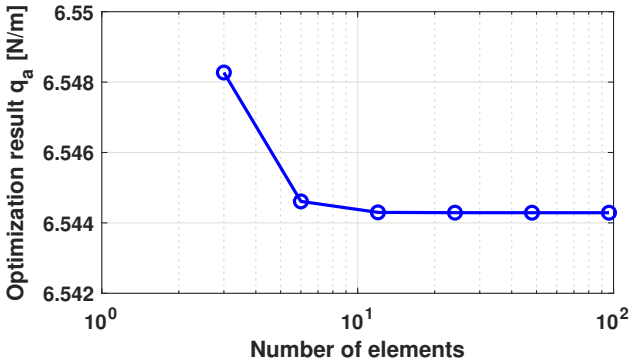

Fig. 16 Influence of the number of finite elements on the optimization result for q_a

After the amplitude of the dynamic motion of the finite element degrees of freedom $\boldsymbol{\xi}_a$ is determined from the result for q_a with Eq. 16, the dynamic behavior of the finite element model degrees of freedom is given as $\boldsymbol{\xi}_a e^{i\omega_g t+\varphi}$, where the phase was aligned with the sinusoidal fit of the marker measurements, as shown in Fig. 14 so that $\varphi = 0$.

From this result for $\boldsymbol{\xi}(t)$, the continuous time-dependent deflection $w(z,t)$ is calculated with the Hermite spline interpolation for each time step. Then, the shear force $Q(z,t)$ and bending moment $M(z,t)$ along the span are obtained with Eq. 12 and 13 from the deflection by using a second-order accurate finite difference scheme. With the results of this procedure, the dynamic component of the shear force and the bending moment for comparison with the dynamic component of the balance measurements can be computed over the period. The comparison is shown in Fig. 17, where the mean value has been subtracted from the balance measurements.

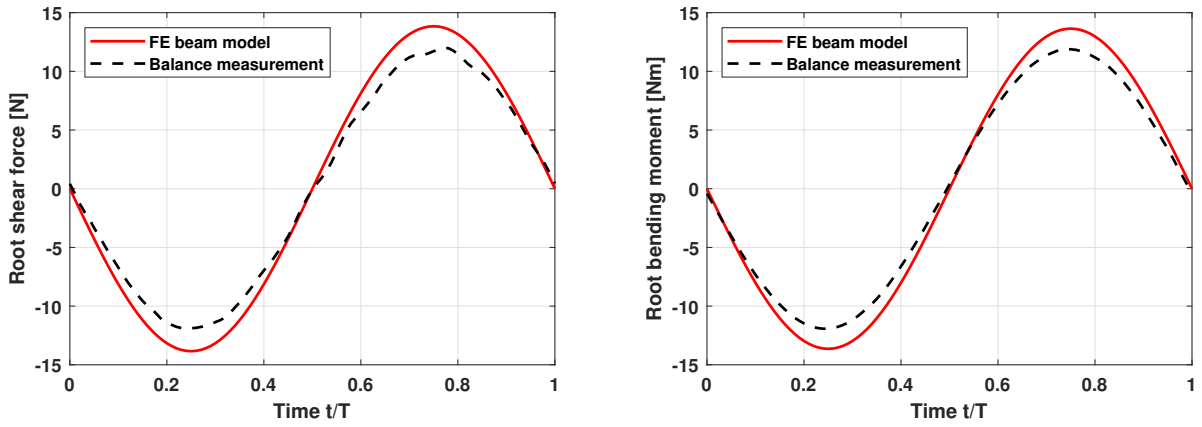

Fig. 17 Comparison of the dynamic component of the root shear force and bending moment from the finite element model with the balance measurements

The RMS value of the difference between model and measurement is 1.43 N for the shear force and 1.26 N m for the bending moment, corresponding to a relative error of 17.10% and 15.01%, respectively, using the RMS of the balance measurements as a reference. The phase alignment between the model and the measurement is very good for both the force and the moment, with phase differences obtained by cross-correlation of the signals of less than 0.5% of the period. The difference in amplitude is therefore concluded to be the only considerable source of error in the finite element model results.

3. Aerodynamic Force

The phase-averaged unsteady flow field and the corresponding wing position as determined from the marker tracks is shown in Fig. 18, for four phase instants over the period. The effect of the gust generator actuation is evident in the plots, with a visibly enlarged or reduced region of accelerated flow over the suction surface of the wing at $t/T = 0.25$ and $t/T = 0.75$, respectively. The level of random error in the phase-averaged measurements of the unsteady periodic inflow is increased compared to the steady flow field that was shown in Fig. 12, because the number of particle tracks in the ensemble-averaging is approximately 15 times smaller, as a result of the data acquisition and processing strategy, where for the steady case 15,000 images were acquired, whereas in the test case with unsteady periodic inflow, only 985 images are available for a time span of 1% of the period.

The calculation of the unsteady lift with Eq. 4 requires the determination of the circulation distribution on the airfoil over the entire period. The circulation distribution $\Gamma(x,t)$ is obtained by performing line integrals of the measured velocity, as defined in Sec. III, for each phase instant. Similar to the test case with steady inflow, the position of the integration path is varied to reduce the effect of the random error in the flow velocity measurements on the result for the circulation. However, in this case, only the positions of the line segments that are upstream, above and below the airfoil are varied, while the downstream segment remains fixed at the particular x-location on the airfoil, to determine the value of $\Gamma(x,t)$ on that respective location. To determine the overall bound circulation around the airfoil $\Gamma(t)$, the downstream segment of the integration path also remains fixed just behind the trailing edge of the airfoil, so that the varying circulation that is shed into the wake in the unsteady case following Kelvin's theorem is not affecting the determined result for the bound circulation $\Gamma(t)$. The line integrals are performed for all spanwise positions where the flow field was measured, and afterwards, the circulation is averaged across the span in the region z_1 to z_2 so that the average lift per unit span on the investigated wing segment is determined with this approach. To further reduce the random error in the measurement, the determined time series of $\Gamma(x,t)$ is fitted with a sinusoidal curve for each chordwise position. The result is shown for four different phase instants in Fig. 19.

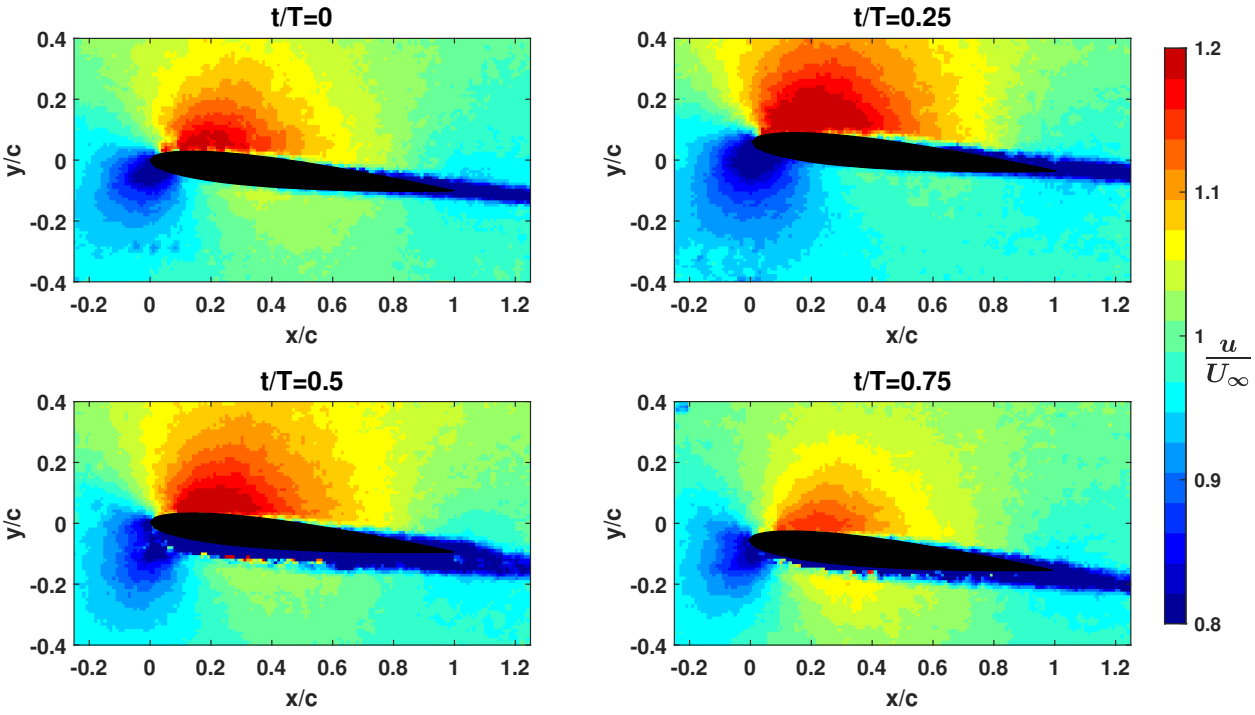

Fig. 18 Flow field and model position at $z/s = 0.875$ for four different phase instants

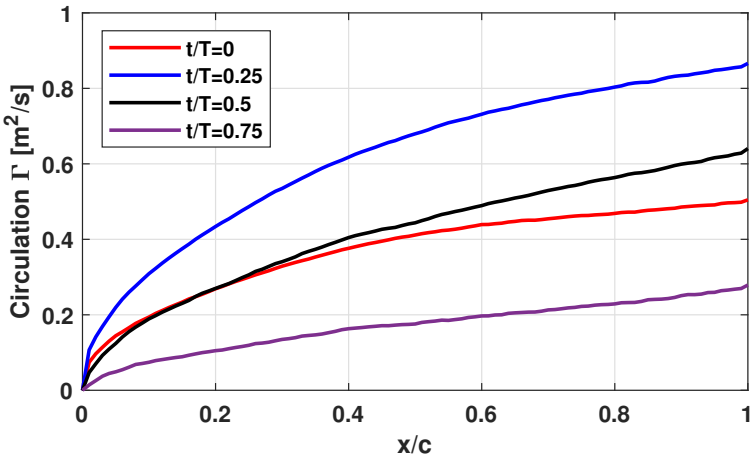

Fig. 19 Distribution of the circulation on the airfoil, as determined by line integrals of the flow velocity

By using Eq. 1 together with the overall bound circulation around the airfoil $\Gamma(t)$, as determined from the unsteady flow fields, the quasi-steady lift is obtained. To determine the unsteady lift, the additional flow acceleration term is computed from the time series of the circulation distribution with Eq. 4. Both lift curves over the period are shown in Fig. 20. The unsteady lift curve as determined from the sinusoidal fit is similar to the quasi-steady lift curve. As a result of including the flow acceleration term in Eq. 4, the amplitude of the unsteady lift is decreased by 0.7% compared to the quasi-steady lift, and the curve is shifted by -2.70% of the period. Considering the linear elastic theory, it is expected that the lift, which acts as the external forcing on the wing, is in phase with the dynamic motion. The lag of the lift with respect to the dynamic motion of the wing is therefore reduced from 3.62% to 0.92% of the period, which follows from including the flow acceleration term, that leads the quasi-steady lift in phase. Therefore, it is noted that including the flow acceleration term reduces the error in phase to less than 1% of the period and hence leads to a significant improvement in the accuracy of the determined lift in the unsteady aeroelastic test case.

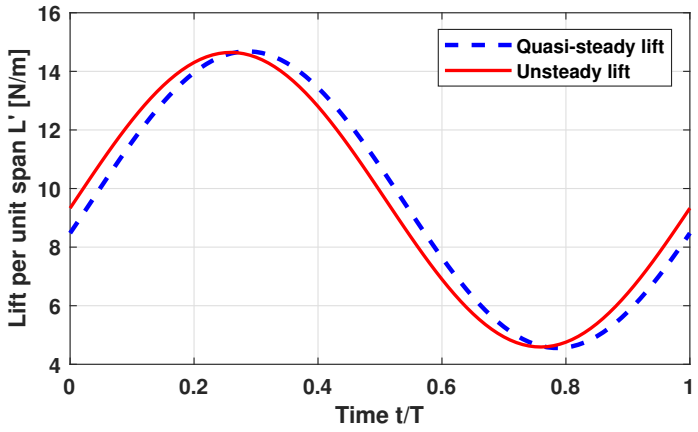

Fig. 20 Quasi-steady and unsteady lift over the period, with steady inflow reference lift

4. Closure of Collar's Triangle

After the three forces in the dynamic aeroelastic interaction are determined based on the PTV measurements, the results can be compared with each other to validate the physical models based on the equilibrium of forces. The aerodynamic and inertial forces on the segment are determined directly with an integration of the obtained results from z_1 to z_2. For the determination of the elastic force on the segment, the amplitude of the dynamic motion of the finite element degrees of freedom $\boldsymbol{\xi}_a$ is combined with the solution in the case of steady inflow $\boldsymbol{\xi}_0$ to yield the dynamic result $\boldsymbol{\xi}(t) = \boldsymbol{\xi}_0 + \boldsymbol{\xi}_a e^{i\omega_g t+\varphi}$, that is used to calculate the shear forces $Q(z_1, t)$ and $Q(z_2, t)$ with finite differences. The results for the three forces on the investigated wing segment are shown in Fig. 21. Additionally, the value of the residual δ is shown over the period.

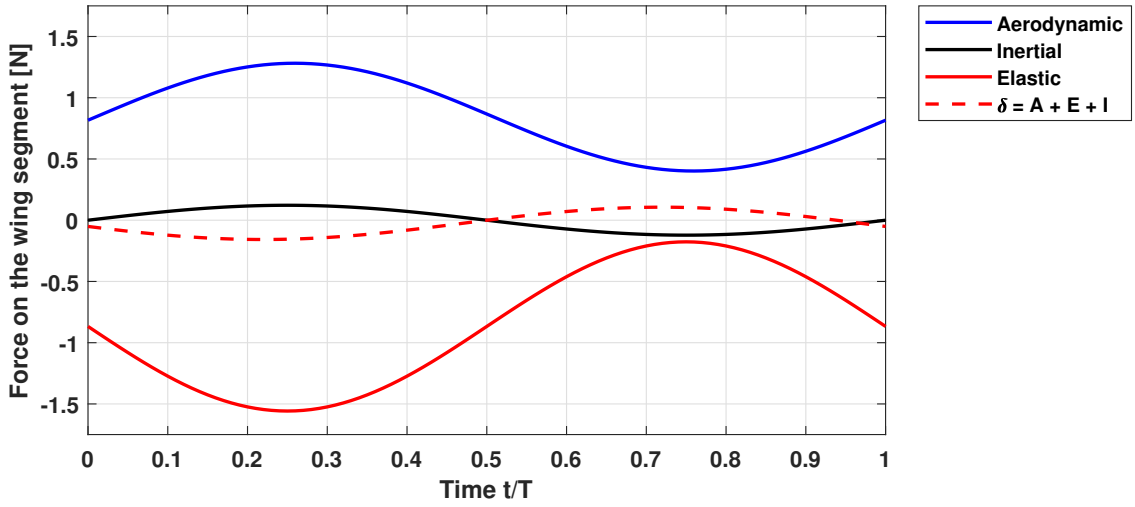

Fig. 21 Collar's triangle of forces as determined from the PTV measurements

The maximum absolute value of δ over the period is 0.158 N at $t/T = 0.23$, which is near the maximum values of the elastic and aerodynamic force magnitudes. The RMS value of δ over the period is 0.0964 N, which corresponds to an error of 11.72% of the reference force from the balance, which is the mean value over the period of the measured root shear force, scaled by the fraction of the investigated wing section. This value of the error in the dynamic aeroelastic test case is very similar to the value of the error in the static aeroelastic test case. It can therefore be assumed that the sources of error are the same as in the static case, especially when considering that the result from the static test case has been used to obtain the result for the dynamic shear force. As a consequence, it is noted that the added complexity of the dynamic test case, with considerable unsteady aerodynamic and inertial forces, is suitably accounted for with the applied methods and does not lead to significant additional sources of error.

VII. Conclusion

This study demonstrated the possibility to fully characterize the aeroelastic response of a flexible wing, in terms of all three force components in Collar's triangle, based on non-intrusive PTV measurements with a single measurement and data processing system. To perform the measurements of the aeroelastic interaction between the flexible wing and the flow, the freestream was seeded with HFSB and the flexible wing model was painted with a grid of fiducial markers. The optical measurements of the flow and the structure were conducted with a CVV probe mounted on a robotic arm, and both data sets were processed with the PTV algorithm Shake-The-Box. This integrated measurement approach requires minimal instrumentation and therefore provides a strategy that considerably simplifies the simultaneous measurement of the aerodynamic and structural response in aeroelastic experiments.

After applying custom post-processing procedures for the particle tracks of the flow and structure separately, the three different forces in the aeroelastic interaction were determined from the results of the PTV measurements using three different methods. The inertial force was determined as the product of mass and acceleration, while the aerodynamic force was determined with an unsteady potential flow model, and the elastic force was determined with a finite element beam model. The physical agreement between the forces from the three models was similar to the agreement between the elastic force and the reference data from the balance measurements, which supports the results for the aerodynamic and inertial forces, and indicates that the structural model should be calibrated with additional structural measurements of the wing, to achieve a better characterization result.

In this demonstration study, physical models of relatively low fidelity were used to determine the forces from the measurement data. However, the fidelity of the aerodynamic and the structural model that are used to analyze the measurements, which are obtained with the considered integrated measurement approach could be increased if required. This would be necessary in particular in the case of non-linear aerodynamic effects due to flow separation, or large structural deformations that cannot be modeled with the linear theory of small deflections, which were not encountered in the present study.

Acknowledgment

This work has been carried out in the context of the HOMER (Holistic Optical Metrology for Aero-Elastic Research) project that has received funding from the European Union's Horizon 2020 research and innovation programme under grant agreement No. 769237.

References

[1] Livne, E., "Future of Airplane Aeroelasticity," *Journal of Aircraft*, Vol. 40, No. 6, 2003, pp. 1066–1092. https://doi.org/10.2514/2.7218.

[2] Collar, A. R., "The Expanding Domain of Aeroelasticity," *The Aeronautical Journal*, Vol. 50, No. 428, 1946, pp. 613–636.

[3] Pike, E. C., "Manual on Aeroelasticity," Report no. 578, AGARD, 1971.

[4] Tang, D., and Dowell, E., "Experimental Aeroelastic Models Design and Wind Tunnel Testing for Correlation with New Theory," *Aerospace*, Vol. 3, No. 2, 2016. https://doi.org/10.3390/aerospace3020012.

[5] Raffel, M., Willert, C. E., Scarano, F., Kähler, C. J., Wereley, S., and Kompenhans, J., *Particle Image Velocimetry: A Practical Guide*, 3rd ed., Springer International Publishing AG, Cham, Switzerland, 2018. https://doi.org/10.1007/978-3-319-68852-7.

[6] Pan, B., "Digital image correlation for surface deformation measurement: historical developments, recent advances and future goals," *Measurement Science and Technology*, Vol. 29, No. 8, 2018. https://doi.org/10.1088/1361-6501/aac55b.

[7] Marimon Giovannetti, L., Banks, J., Turnock, S. R., and Boyd, S. W., "Uncertainty assessment of coupled Digital Image Correlation and Particle Image Velocimetry for fluid-structure interaction wind tunnel experiments," *Journal of Fluids and Structures*, Vol. 68, 2017, pp. 125–140. https://doi.org/10.1016/j.jfluidstructs.2016.09.002.

[8] Zhang, P., Peterson, S. D., and Porfiri, M., "Combined particle image velocimetry/digital image correlation for load estimation," *Experimental Thermal and Fluid Science*, Vol. 100, 2019, pp. 207–221. https://doi.org/10.1016/j.expthermflusci.2018.09.011.

[9] Liu, T., Montefort, J., Gregory, J., Palluconi, S., Crafton, J., and Fonov, S., "Wing Deformation Measurements from Pressure Sensitive Paint Images Using Videogrammetry," *41st AIAA Fluid Dynamics Conference and Exhibit*, 2011, pp. 1–31. https://doi.org/10.2514/6.2011-3725.

[10] Schanz, D., Gesemann, S., and Schröder, A., "Shake-The-Box: Lagrangian particle tracking at high particle image densities," *Experiments in Fluids*, Vol. 57, No. 5, 2016. https://doi.org/10.1007/s00348-016-2157-1.

[11] Scarano, F., Ghaemi, S., Caridi, G. C. A., Bosbach, J., Dierksheide, U., and Sciacchitano, A., "On the use of helium-filled soap bubbles for large-scale tomographic PIV in wind tunnel experiments," *Experiments in Fluids*, Vol. 56, No. 2, 2015. https://doi.org/10.1007/s00348-015-1909-7.

[12] Huhn, F., Schanz, D., Gesemann, S., Dierksheide, U., van de Meerendonk, R., and Schröder, A., "Large-scale volumetric flow measurement in a pure thermal plume by dense tracking of helium-filled soap bubbles," *Experiments in Fluids*, Vol. 58, No. 9, 2017. https://doi.org/10.1007/s00348-017-2390-2.

[13] Martínez Gallar, B., van Oudheusden, B. W., Sciacchitano, A., and Karásek, M., "Large-scale volumetric flow visualization of the unsteady wake of a flapping-wing micro air vehicle," *Experiments in Fluids*, Vol. 61, No. 1, 2019. https://doi.org/10.1007/s00348-019-2854-7.

[14] Wolf, C. C., Schwarz, C., Kaufmann, K., Gardner, A. D., Michaelis, D., Bosbach, J., Schanz, D., and Schröder, A., "Experimental study of secondary vortex structures in a rotor wake," *Experiments in Fluids*, Vol. 60, No. 11, 2019. https://doi.org/10.1007/s00348-019-2807-1.

[15] Mitrotta, F. M. A., Sciacchitano, A., Sodja, J., de Breuker, R., and van Oudheusden, B. W., "Experimental investigation of the fluid-structure interaction between a flexible plate and a periodic gust by means of Robotic Volumetric PIV," *13th International Symposium on Particle Image Velocimetry*, edited by C. J. Kähler, R. Hain, S. Scharnowski, and T. Fuchs, 2019, pp. 645–656. https://doi.org/https://doi.org/10.18726/2019_3.

[16] van Oudheusden, B. W., "PIV-based pressure measurement," *Measurement Science and Technology*, Vol. 24, No. 3, 2013. https://doi.org/10.1088/0957-0233/24/3/032001.

[17] Rival, D. E., and van Oudheusden, B. W., "Load-estimation techniques for unsteady incompressible flows," *Experiments in Fluids*, Vol. 58, No. 3, 2017. https://doi.org/10.1007/s00348-017-2304-3.

[18] Gherlone, M., Cerracchio, P., and Mattone, M., "Shape sensing methods: Review and experimental comparison on a wing-shaped plate," *Progress in Aerospace Sciences*, Vol. 99, 2018, pp. 14–26. https://doi.org/10.1016/j.paerosci.2018.04.001.

[19] Anderson Jr., J. D., *Fundamentals of Aerodynamics*, 5th ed., McGraw-Hill, New York, USA, 2011.

[20] Lind, A. H., Lefebvre, J. N., and Jones, A. R., "Time-Averaged Aerodynamics of Sharp and Blunt Trailing-Edge Static Airfoils in Reverse Flow," *AIAA Journal*, Vol. 52, No. 12, 2014, pp. 2751–2764. https://doi.org/10.2514/1.J052967.

[21] Lee, T., and Su, Y. Y., "Low Reynolds number airfoil aerodynamic loads determination via line integral of velocity obtained with particle image velocimetry," *Experiments in Fluids*, Vol. 53, No. 5, 2012, pp. 1177–1190. https://doi.org/10.1007/s00348-012-1353-x.

[22] Katz, J., and Plotkin, A., *Low-Speed Aerodynamics*, 2nd ed., Cambridge University Press, New York, USA, 2001.

[23] Mitrotta, F. M. A., Rajpal, D., Sodja, J., and De Breuker, R., "Multi-Fidelity Design of an Aeroelastically Tailored Composite Wing for Dynamic Wind Tunnel Testing," *AIAA SciTech Forum*, AIAA, 2020, pp. 1–26. https://doi.org/10.2514/6.2020-1636.

[24] Hodges, D. H., and Pierce, G. A., *Introduction to Structural Dynamics and Aeroelasticity*, 2nd ed., Cambridge University Press, New York, USA, 2011.

[25] Lancelot, P. M. G. J., Sodja, J., Werter, N. P. M., and Breuker, R. D., "Design and testing of a low subsonic wind tunnel gust generator," *Advances in aircraft and spacecraft science*, Vol. 4, No. 2, 2017, pp. 125–144. https://doi.org/10.12989/aas.2017.4.2.125.

[26] Leishman, J. G., *Principles of Helicopter Aerodynamics*, 2nd ed., Cambridge University Press, New York, USA, 2006.

[27] Faleiros, D. E., Tuinstra, M., Sciacchitano, A., and Scarano, F., "Generation and control of helium-filled soap bubbles for PIV," *Experiments in Fluids*, Vol. 60, No. 3, 2019. https://doi.org/10.1007/s00348-019-2687-4.

[28] Schneiders, J. F. G., Scarano, F., Jux, C., and Sciacchitano, A., "Coaxial volumetric velocimetry," *Measurement Science and Technology*, Vol. 29, No. 6, 2018. https://doi.org/10.1088/1361-6501/aab07d.

[29] Jux, C., Sciacchitano, A., Schneiders, J. F. G., and Scarano, F., "Robotic volumetric PIV of a full-scale cyclist," *Experiments in Fluids*, Vol. 59, No. 4, 2018. https://doi.org/10.1007/s00348-018-2524-1.

[30] Schanz, D., Gesemann, S., Schröder, A., Wieneke, B., and Novara, M., "Non-uniform optical transfer functions in particle imaging: calibration and application to tomographic reconstruction," *Measurement Science and Technology*, Vol. 24, No. 2, 2013. https://doi.org/10.1088/0957-0233/24/2/024009.

[31] Sciacchitano, A., and Scarano, F., "Elimination of PIV light reflections via a temporal high pass filter," *Measurement Science and Technology*, Vol. 25, No. 8, 2014. https://doi.org/10.1088/0957-0233/25/8/084009.

[32] Wieneke, B., "Volume self-calibration for 3D particle image velocimetry," *Experiments in Fluids*, Vol. 45, No. 4, 2008, pp. 549–556. https://doi.org/10.1007/s00348-008-0521-5.

[33] Agüera, N., Cafiero, G., Astarita, T., and Discetti, S., "Ensemble 3D PTV for high resolution turbulent statistics," *Measurement Science and Technology*, Vol. 27, No. 124011, 2016, p. 12pp. https://doi.org/10.1088/0957-0233/27/12/124011.